



OPEN

SUBJECT AREAS:
SOLAR CELLS
POROUS MATERIALS
PHOTOCATALYSISReceived
30 May 2014Accepted
23 September 2014Published
28 October 2014Correspondence and
requests for materials
should be addressed to
J.H.M. (junhyuk@
sogang.ac.kr)

Facile fabrication of sub-100 nm mesoscale inverse opal films and their application in dye-sensitized solar cell electrodes

Jung Woo Lee, Jaemin Lee, Cheolho Kim, Chang-Yeol Cho & Jun Hyuk Moon

Department of Chemical and Biomolecular Engineering, Sogang University, Seoul 121-742, Republic of Korea.

Inverse opal (IO) films with mesoporous structures hold promise as high-performance electrodes for various photoelectrochemical devices because of their high specific area as well as their fully connected pore structure. A great challenge to their use is obtaining an intact film of mesoscale colloidal crystals as a template. Here, using the plate-sliding coating method coupled with hot air flow, we successfully deposited mesoscale colloidal crystals onto the substrate. A TiO₂ mesoscale IO (meso-IO) with 70 nm pores was then successfully fabricated via atomic layer deposition of TiO₂ and subsequent removal of the template. As a photoelectrochemical electrode, the meso-IO structure exhibits enhanced charge transport properties as well as a high specific area. Moreover, dye-sensitized solar cells fabricated using the meso-IO electrode exhibit a higher photocurrent and cell efficiency than a cell constructed using a conventional TiO₂ nanoparticle electrode. This meso-IO film provides a new platform for developing electrodes for use in various energy storage and conversion devices.

Photoelectrochemical devices, including hydrogen-generation cells and thin-film or dye-sensitized solar cells, have received much attention recently because of their ability to harness solar energy, a form of renewable energy^{1,2}. Dye-sensitized solar cells (DSCs), in particular, are one of the most promising next-generation devices because of their high photon-to-electricity conversion efficiency and low fabrication costs^{3–5}. The electrodes conventionally used in these devices are typically composed of randomly packed TiO₂ nanoparticles, forming a nanoparticulate (NP) film. These structures have been widely used because their large specific area allows for a high adsorption density of sensitizing dyes or nanoparticles, thereby leading to a high photoelectron density. However, their random pathway as well as the multiple trapping and de-trapping transport steps that occur because of particle arrangement slow charge diffusion and may result in large photocurrent loss by charge recombination^{6,7}. Researchers have recently therefore attempted to create ordered electrode structures, such as arrays of nanotubes or nanowires, pore-patterned structures and inverse opal (IO) structures^{8–12}.

The IO structure produced by colloidal crystals has been widely studied because of its fully connected skeleton and controlled pore structure. IO-based fabrication offers a high degree of morphology tunability, including the formation of core-shell or multi-shell structures, as well as greater control over pore size, from submicrometer to a few-micrometer dimensions^{13,14}. Additionally, the connected structure of IO imparts it with better electron transport properties compared to those of disordered conventional electrode materials. In previous studies, our group has observed that the recombination lifetime of DSCs containing TiO₂-based IO electrodes was 6-times longer than that of the TiO₂ NP electrodes¹⁵. Moreover, the ordered macroporous structures of IO make it easier to fill its pores with electrolyte solutions or polymeric electrolytes¹⁶. Additionally, the periodic contrast of dielectric constants in the IO structure can lead to the manifestation of a photonic bandgap property, enhancing the light-harvesting efficiency of DSCs and photocatalysts¹³. Despite these promising characteristics, IO-based structures have not yet delivered high performance in the aforementioned applications. One of the limitations preventing the successful use of IO electrodes is their low specific area, which arises from the macroscale dimensions of their pores. Most of the IO fabricated in the aforementioned studies mentioned had pore sizes in the range of several hundred nanometers to a few micrometers. IO films with 550–600 nm diameter macropores have a specific area, as evaluated by the dye adsorption density, approximately 10 times lower than that of NP films¹⁵. Some authors have proposed techniques for decorating the surface of IO frameworks with nanopar-

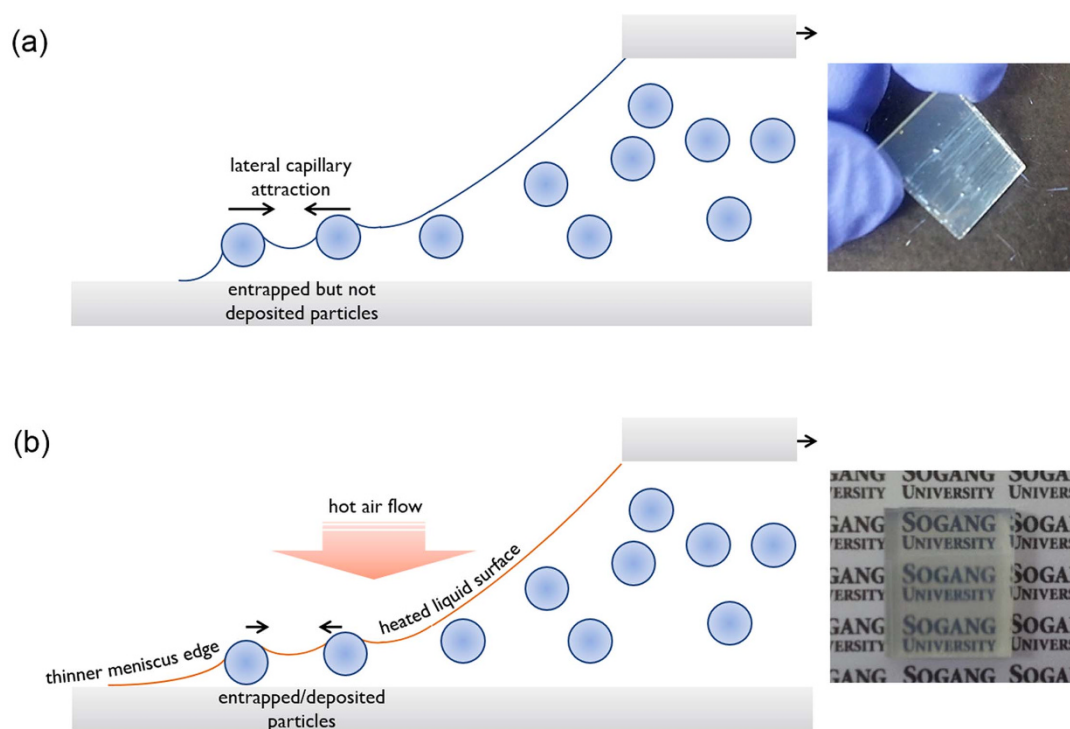


Figure 1 | Comparative diagram of the self-assembly of small particles (a) without and (b) with hot air flow using the plate-coating approach. A photograph of the resulting colloidal crystal film on the substrate is also shown for each approach.

ticles or nanorods to overcome this issue. However, the decoration of nanorods increases the specific area to only 30–40% of the area of NP films¹⁴. Additionally, the decoration approach has been observed to limit the increase of specific area because excessive growth blocks the macropores of the IO structure¹⁴.

In this work, we present mesoscale-pore IO (meso-IO) structures with sub-100 nm pores for use as electrodes in photoelectrochemical devices. Here, we designate pores with diameters smaller than 100 nm as mesoscale pores. (This definition of a mesopore differs from that of IUPAC, which defines mesopores as pore sizes between 10 and 50 nm.) We directly scaled down the pore size of the IO by utilizing colloidal crystal templates of sub-100 nm polystyrene (PS) particles with the aim of enhancing its specific surface area. The fabrication of an intact film using particles with small diameters is particularly difficult because their tendency to trap particles at the edge of the meniscus is low during the coating process. Here, using the plate-sliding coating method with convective hot air flow, we successfully deposited mesoscale colloidal crystals onto the substrate. A TiO₂ meso-IO film with 70 nm pores was successfully fabricated by atomic layer deposition of TiO₂ and subsequent removal of the template. To evaluate the electrode performance of the meso-IO structures, we tested them alongside conventional NP TiO₂ electrodes as the photoelectrodes of DSCs. We observed that the dye-adsorption density of the meso-IO was up to 77% that of the NP film, which was at least twice that achieved using the aforementioned decoration approaches. Moreover, the meso-IO structures exhibited faster charge transport properties than NP electrodes with a similar electrode thickness. When utilized in a DSC, the meso-IO displayed 15% higher efficiency as a 5.6- μm thick electrode. The meso-IO structures have the potential to be used in various photoelectrochemical devices. Their mesoscale pore features may also be beneficial when used in recently reported solid-state DSCs based on perovskite-sensitized cells, which often require electrodes that are less than 1 μm thick^{17,18}.

Results

Fabrication of mesoscale colloidal crystal films and mesoscale inverse opals. Dip-coating or plate-sliding coating has been widely used to fabricate colloidal crystal films¹⁹. Colloidal crystals were formed according to the following process: particles near the edge of the meniscus were pinned onto the substrate, and particles that were continuously drawn toward this edge by the convective flow were assembled by the lateral capillary force induced by the concave meniscus between the spheres. The preparation of an intact film using particles of small diameter was difficult with this process because the tendency to trap such particles at the edge of the meniscus is low (see Figure 1)²⁰. The small particles assembled in the liquid phase rather than on the substrate, resulting in the delamination of the colloidal crystal film from the substrate, as displayed in the photograph in Figure 1a. In this study, we utilized the plate-sliding coating approach with hot air flowed directly into the meniscus region (50–60°C; flow rate: 5–8 m s⁻¹). The hot-air flow heated the colloidal solution, reducing the thickness of the meniscus because of the rapid evaporation of solvent and the decrease of the surface tension of the liquid. The contact angle of the polystyrene (PS) colloidal solution heated at 60°C was 52°–56°, whereas the contact angle was 67° at room temperature. The surface tension of the PS colloidal solution at 60°C was approximately 10% lower than that at room temperature. As described in Figure 1b, this lower surface tension may lead to an increase in the rate of particles entrapped prior to colloidal crystallization. Moreover, the decrease in the surface tension of liquids at high temperatures may enhance the lateral capillary force between particles, resulting in weakly aggregated colloidal crystals²⁰. Relatively weak aggregation reduces the compressive stress of colloidal crystal films, resulting in a more intact coating of colloidal crystals on the substrate. The photograph in Figure 1b clearly shows the intact film of the PS colloidal crystal film on the substrate.

Figures 2a and 2b show SEM images of the cross-section of a mesoscale PS colloidal crystal film. We controlled the thickness of



the PS colloidal crystal film by varying the rate of plate sliding and successfully fabricated films with thicknesses of up to approximately $5.6\ \mu\text{m}$ by altering the initial rate of substrate movement of $0.15\ \text{cm s}^{-1}$. When the thickness was greater than approximately $6\ \mu\text{m}$, we often observed delamination, which we attributed to high compressive stress in the colloidal crystal films of small spheres. The PS colloidal crystals formed were utilized as templates, and TiO_2 was subsequently deposited using the atomic layer deposition (ALD) technique with TiCl_4 and water vapor as precursors²¹. The vapor-phase deposition of oxide films allows complete infiltration and a more stoichiometric reaction between precursors. Moreover, the relatively high temperature and vacuum environment in the ALD process allows for the facile removal of volatile moieties (e.g., water) incorporated into the oxide film during synthesis. A cross-sectional SEM image of the TiO_2 meso-IO after the removal of the PS colloidal crystal template is shown in Figure 2c, and a complete IO skeleton throughout the film thickness is clearly observed. The meso-IO TiO_2 possessed an anatase dominant phase, as shown in Figure S1. The pore size in the meso-IO structure is approximately $70\ \text{nm}$ in diameter, as shown in the magnified inset image. The pore size shrunk by 30%; however, the pore-pore distance was approximately $80\ \text{nm}$. The decrease in pore size was partially induced by an increase in the TiO_2 shell thickness during the crystallization of TiO_2 upon oxidative heat-treatment rather than overall film shrinkage. In the photograph of the TiO_2 meso-IO films (Figure 1d), no macroscopic cracks or delamination is evident. The photograph shows a transparent film similar to the PS colloidal crystal film, which is attributed to low Mie back-scattering of visible light by the mesoscale pore features. Figure S2 shows a plot of the simulated scattering as a function of the pore size of the TiO_2 matrix. The intensity of the back-scattering was observed to be especially weak for pore sizes less than $100\ \text{nm}$.

We characterized the optical properties of the meso-IO films by collecting their transmittance and diffuse reflectance spectra using a UV-Vis spectrophotometer, as shown in Figure 3. The transmittance and reflectance values of the NP TiO_2 film are presented for comparison. In Figure 3a, the transmittance of the meso-IO film was, on average, 45% over the wavelength range of $400\text{--}700\ \text{nm}$, whereas the transmittance of the NP film was greater than 85%. Meanwhile, the

diffuse reflectance of the meso-IO film was, on average, 18%, whereas that of the NP film was, on average, 8% (Figure 3b). Thus, we observed that the normal transmittance of the meso-IO film was relatively low considering the difference in reflectance between the meso-IO and NP films. This result implies that the mesoscale pores in the meso-IO film exhibit high forward scattering, i.e., diffuse transmittance, as shown in Figure S2.

Here, we estimated the surface area of the meso-IO films spectrophotometrically by measuring the concentration of adsorbed dye. Specifically, the molar amounts of sensitizing dye N719 adsorbed onto the surface of TiO_2 films were calculated. The density of dye adsorption per unit film area for the meso-IO and NP electrodes was $0.040\ \mu\text{mol cm}^{-2}$ and $0.052\ \mu\text{mol cm}^{-2}$, respectively. Thus, the specific area of the meso-IO films can be regarded as 77% that of the NP structures.

Characterization of charge transport properties of meso-IO structures. The charge transport properties of the meso-IO TiO_2 films were characterized using the intensity-modulated voltage spectroscopy (IMVS) and intensity-modulated photocurrent spectroscopy (IMPS) techniques. The charge transport time and recombination lifetime were obtained and used to determine the charge-collection efficiency, which determines the photocurrent density and cell efficiency of cells constructed using these films. In this study, the charge transport time and the recombination lifetime were obtained with various incident photon fluxes. Figure 4a shows the typical IMPS responses obtained for the two electrodes at a photon flux of $1.32 \times 10^{16}\ \text{cm}^{-2}\text{s}^{-1}$. The charge transport time (τ_t) was estimated from the frequency minimum (f_{min}) of the IMPS imaginary component, $\tau_t = 1/2\pi f_{min}$ ²². Figure 4b shows the electron transit time at various photon fluxes, as derived from the IMPS curves. These results indicate that the electron transit time of the meso-IO film was approximately 30% shorter than that of the NP film over the measured range of photon flux. The charge transport time τ_t is known to depend on the specific area of the electrode film. The value of τ_t moderately increases as the surface area of the electrode increases. Because the NP film had a surface area 1.25-times greater than that of the meso-IO film, determination of the

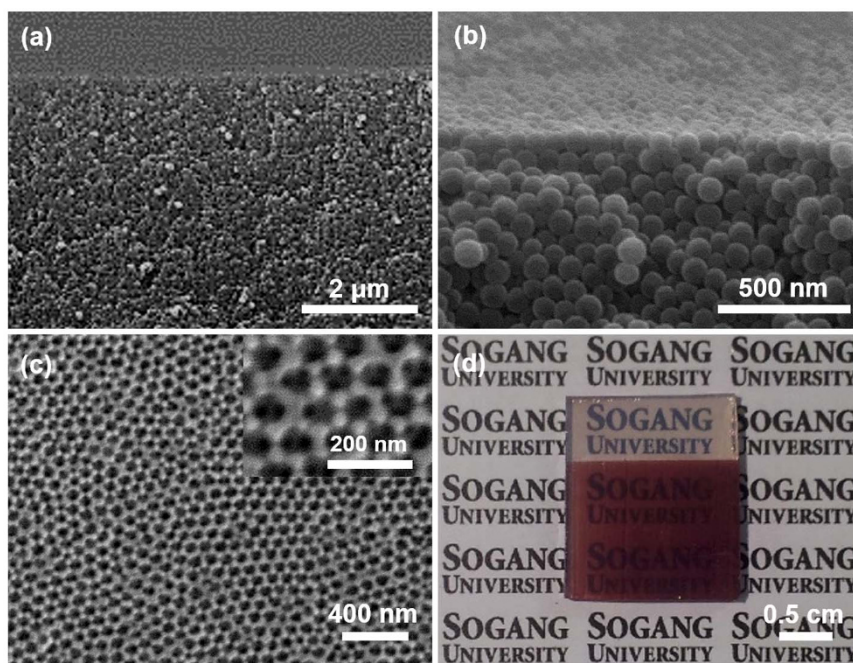


Figure 2 | Visual characterization of the mesoscale PS colloidal crystal film, showing (a) an SEM image of the cross-section and (b) a magnified SEM image of the cross-section. The inset shows a photograph of the film. (c) SEM image of a cross-section of the TiO_2 meso-IO film; the inset shows the magnified pore structures. (d) Photograph of a TiO_2 meso-IO film. Here, the film was sensitized by N719 dye.

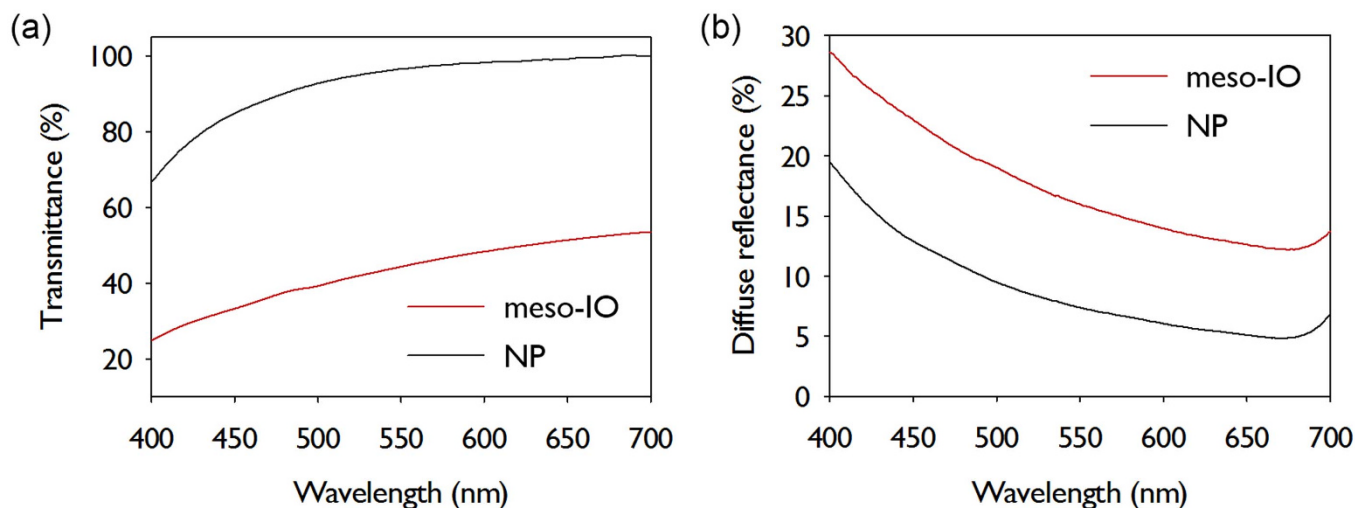


Figure 3 | (a) UV-Vis transmittance and (b) diffuse reflectance of the meso-IO and NP films.

surface-area-normalized transit time was necessary to evaluate the meso-IO electrode against the NP electrode. The charge transport time τ_t has previously been reported to be related to the volumetric trap density N_t by the relationship $\tau_t \propto N_t^{2/3}$ ²³. This equation can be further modified to $\tau_t \propto (\text{specific area})^{2/3}$ because the trap state was reported to be predominantly located on the TiO₂ surface^{23,24}. Using this relationship, we estimated the surface-area-normalized τ_t of the meso-IO film to be 20% shorter than that of the NP film.

Figure 4c shows the typical IMVS responses for the meso-IO and NP TiO₂ films at a photon flux of $1.32 \times 10^{16} \text{ cm}^{-2}\text{s}^{-1}$. The recombination lifetimes (τ_r) that were obtained from the frequency minimum of the IMPS imaginary component, $\tau_r = 1/2\pi f_{\text{min}}$, of the meso-IO and NP films are shown in Figure 4d as a function of the incident photon flux²². At a photon flux of $1.32 \times 10^{16} \text{ cm}^{-2}\text{s}^{-1}$, the τ_r of the meso-IO film was $6.34 \times 10^{-3} \text{ s}$, which is approximately 26% longer than that of the NP film. Similar to the transit time, the electron lifetime also depends on the specific area. An increase in the specific area of the electrode film resulted in a shortened recombination lifetime. Empirical fitting of recombination current density as a function of specific area has been reported to reveal the relationship $\tau_r \propto (\text{specific area})^{-0.33}$ ²⁵. We obtained the surface-area-normalized τ_r on the basis of this relationship; the τ_r of the meso-IO film was approximately 16% longer than that of the NP film.

As a brief summary, the meso-IO structures exhibited an enhanced charge transit time and recombination lifetime compared to the conventional NP structures. The meso-IO skeleton displays less particulate than the NP structures. (see Figure S3), which may contribute to this enhancement²⁶. The collection efficiency (η_{col}) can be determined by the equation $\eta_{\text{col}} = 1 - (\tau_t/\tau_r)$ for a high charge-collection efficiency device (approximately $> 95\%$)²². The η_{col} of the meso-IO electrode was 94%, whereas that of the NP electrode was 90% at a photon flux of $1.32 \times 10^{16} \text{ cm}^{-2}\text{s}^{-1}$. Considering the same specific areas of these electrodes, we estimated the η_{col} of the meso-IO electrode and the NP electrode to be 94% and 89%, respectively; thus, the meso-IO electrode exhibits a η_{col} that is 5% higher than that of the NP electrode.

Application of TiO₂ meso-IO electrodes in DSCs. A DSC incorporating the meso-IO electrodes was assembled, and the photocurrent density vs. voltage (J - V) was characterized under AM 1.5G illumination; the results are shown in Figure 5. The J - V performance of the NP TiO₂ electrodes was measured for comparison. Two different thicknesses of meso-IO (2.6 μm and 5.6 μm) and NP (2.5 μm and 5.6 μm) electrodes were fabricated.

Table 1 lists the J - V parameters measured for the DSCs, including the J_{sc} (short-circuit current), V_{oc} (open-circuit voltage), FF (fill factor), and the calculated overall conversion efficiency (η). Among these parameters, the J_{sc} values of the meso-IO-electrode DSCs were approximately 15% and 20% higher than those of the NP-electrode DSCs of similar thickness, respectively. Moreover, the meso-IO DSCs exhibited a 1.8-fold increase in the J_{sc} when the electrode thickness was increased 2.2-fold. The ratio between the increase in J_{sc} and the increase in film thickness was 0.82, whereas this ratio for the NP electrode DSCs was 0.75. With increasing electrode film thickness, the collection efficiency is more affected by the intrinsic charge transport properties of the electrode²⁷. Thus, the higher ratio of the meso-IO electrode implies higher collection efficiency for these electrodes than for the NP electrodes. This result qualitatively corresponds to the previously discussed comparison of collection efficiencies. Moreover, this result also implies that, with thicker electrode films or higher photocurrent generation conditions, the difference in the J_{sc} between the meso-IO and NP electrodes increases. We prepared thicker films (7 μm) of meso-IO and NP electrodes and sensitized these films with an indoline organic dye (D205) that exhibits a much higher light absorption coefficient than the N719 dye²⁸. Here, we prepared the thick meso-IO TiO₂ film by inverting the multiply coated opal film (see Figure S4). The photocurrents of the meso-IO- and NP-electrode-containing D205-sensitized solar cells were measured to be 15.43 mA cm^{-2} and 11.22 mA cm^{-2} , respectively. The J_{sc} of the meso-IO electrode was 38% higher than that of the NP electrode. Notably, the J_{sc} of the DSC fabricated using the thicker meso-IO electrode with D205-sensitization was much improved compared to that of the thinner and N719-sensitized meso-IO electrode DSC.

Meanwhile, the J_{sc} is explicitly correlated to the efficiencies of (1) the amount of light harvested (η_{lh}) by the electrode, (2) electron injection (η_{inj}) from the dye into the electrode, and (3) electron collection (η_{col}) by the conducting substrate:

$$J_{\text{sc}} = \int q I_0(\lambda) \eta_{\text{lh}}(\lambda) \eta_{\text{col}} \eta_{\text{inj}} d\lambda \quad (1)$$

We estimated that the η_{inj} is similar for the meso-IO and NP TiO₂ electrodes because the same post-treatment of the TiO₂ precursors (0.1 mM TiCl₄ solution, 10 min) was used in the preparation of both electrodes. With respect to the DSCs with 5.6 μm thick electrode films, where the J_{sc} of the meso-IO electrode was 20% greater than that of the NP electrode, we expect that the wavelength-averaged η_{lh} for the meso-IO electrode DSC may be 13.6% higher than that of the

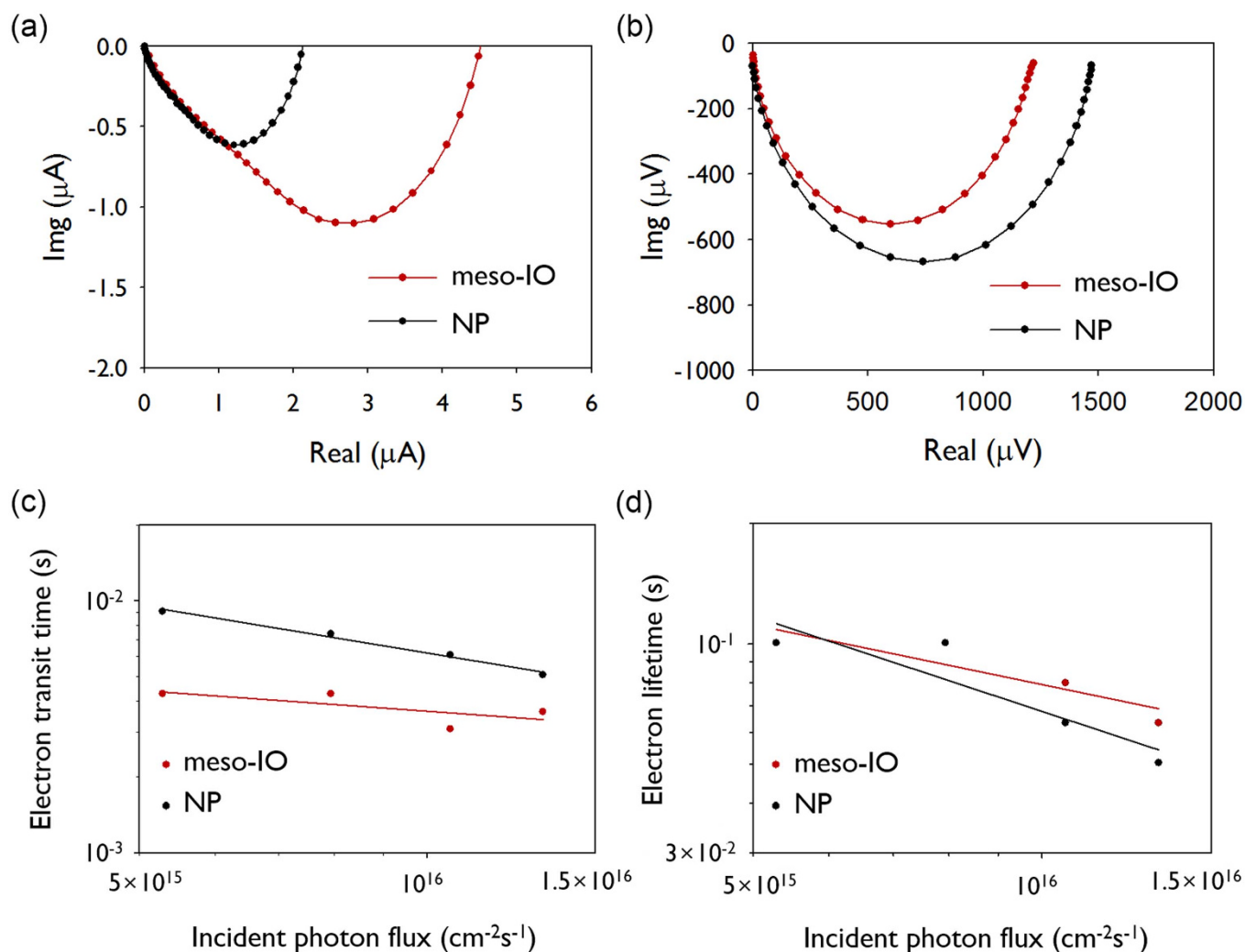


Figure 4 | (a) IMPS and (c) IMVS spectra of the meso-IO and NP films at a photon flux of $1.32 \times 10^{16} \text{ cm}^{-2} \text{ s}^{-1}$. (b) The electron transit time and (d) the electron lifetime at various photon fluxes for these films.

NP electrode because the η_{col} of the meso-IO electrode was 5% higher than that of the NP electrode. Specifically, η_{th} is affected by optical densities, including both the dye adsorption density and the optical

scattering of the electrode. The meso-IO electrode exhibited a lower dye-adsorption density but better visible-light-scattering properties than the NP electrode. Thus, light-scattering ability of the meso-IO electrode may be sufficiently high to compensate for its low specific area, resulting in a 13.6% higher η_{th} .

The V_{oc} of the meso-IO electrode DSCs is 5–6% lower than that of the NP electrode DSCs. This lower V_{oc} may be due to the smaller contact area of the more porous meso-IO with the substrate, resulting in a higher series resistance at the electrode/substrate interface. The FFs of both electrodes DSCs were similar. Finally, the DSC efficiency, η , of the meso-IO electrode was similar to that of the NP electrode in the case of the thin (2.5–2.6 μm) electrode film but was 14% greater than the NP electrode in the case of the thick (5.6 μm) electrode film.

Discussion

Mesoscale colloidal crystals were fabricated by evaporation-induced self-assembly under a hot convective air flow. Slow nucleation deposition, resulting in higher compressive stresses in the self-assembly of small colloidal spheres, was overcome by the rapid-evaporation-assisted deposition of colloidal particles. The ALD of TiO_2 was used to obtain a uniform coating throughout the cavities of the sub-100 nm PS particle assemblies. Using this method, we successfully prepared a TiO_2 IO film approximately 70 nm in diameter. We characterized the UV-Vis transmittance and specific area of this

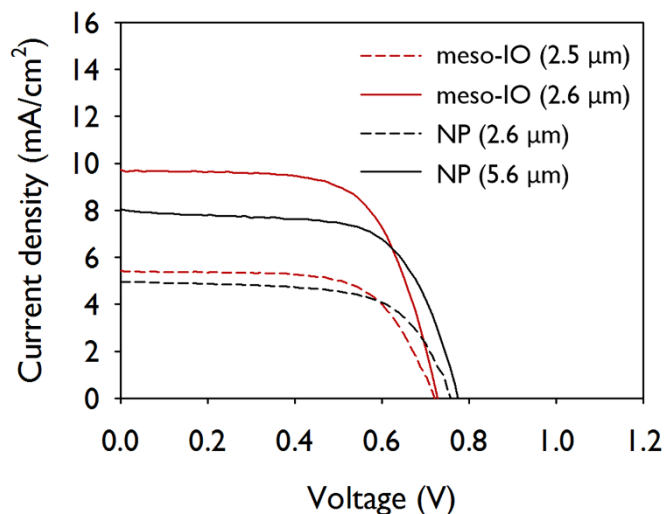


Figure 5 | (a) J - V characteristics of DSCs assembled using meso-IO and NP TiO_2 electrode films.


Table 1 | The photovoltaic parameters and calculated efficiencies of DSCs assembled using meso-IO and NP TiO₂ electrode films

Electrode	Thickness [μm]	J_{sc} [mA cm^{-2}]	V_{oc} [V]	FF	Eff. [%]
meso-IO	2.5	5.41	0.721	0.660	2.579
	5.6	9.72	0.734	0.651	4.647
NP	2.6	4.96	0.761	0.649	2.447
	5.6	8.06	0.774	0.652	4.062

meso-IO TiO₂ film. In contrast to previous IO structures with pore sizes of several hundred nanometers, the meso-IO film exhibits relatively high transparency because of the sub-100 nm cavity size, which reduces Mie back-scattering. The specific area of the meso-IO film, as evaluated on the basis of dye adsorption density, was approximately 77% that of the NP film and was 2–3 times greater than that of the IO-based structures reported previously. The charge collection properties of the meso-IO TiO₂ electrodes were also compared to those of the NP TiO₂ structures. The meso-IO electrodes were estimated to have charge collection efficiency 5% higher than that of the NP electrodes. This higher collection efficiency may be attributable to the more ordered and connected morphology of the IO skeleton. Finally, the meso-IO structures were tested as an electrode for use in liquid-electrolyte DSCs; they exhibited a J_{sc} 15–20% higher than that of the NP-electrode DSCs. We attributed this increased J_{sc} to a higher η_{lh} as well as a higher η_{col} for the meso-IO structures. The meso-IO film can potentially be used as an alternative, high-performance electrode in solar cells for harnessing the sensitization produced by high-extinction-coefficient perovskites or quantum dots that require films thinner (on the order of a few micrometers thick) than those used in DSCs. The well-defined and fully connected porous IO structures may also facilitate the use of polymer electrolytes or hole-conducting polymers in these devices. Furthermore, meso-IO structures that possess a higher specific area compared to that of previous IO structures may be useful in various photoelectrochemical applications, including photocatalysts and water splitting.

Methods

Preparation of meso-IO TiO₂ films. A layer of opals of monodisperse PS particles (99 nm in diameter, 3% polydispersity, Bangs Lab, Inc.) was coated onto fluorine doped tin oxide (FTO) substrates using the sliding-bar coating method with convective air flow at temperatures between 50 and 60 °C. The coating rate (i.e., the substrate withdrawal rate) was approximately 0.2–0.5 cm min⁻¹. TiO₂ deposition was performed using the atomic layer deposition system. Titanium tetrachloride and deionized water were used as precursors and were sequentially fed into the reactor using N₂ gas. A chamber pressure of 0.55 Torr, an exposure time of 15 s, and a purge time of 17 s were used throughout the deposition for both TiCl₄ and water. The TiO₂ deposition rate under these conditions was approximately 0.13 nm cycle⁻¹. Subsequently, the TiO₂-deposited PS opals were heated at 500 °C for 2 h in air to remove the PS template. A reactive-ion etching procedure using a mixture of CF₄ (40 sccm) and O₂ (4 sccm) was used to remove the overcoat. The sample was then post-treated in an aqueous 0.3 M TiCl₄ solution for 20 min, as reported elsewhere. The area of the meso-IO TiO₂ film was controlled via scraping to yield a film area of approximately 9–10 mm².

Assembly of the DSCs. The meso-IO and NP TiO₂ films were sensitized by being immersed for 20 h in a 0.5 mM solution of N719 dye (Dyesol) in anhydrous ethyl alcohol (99.9%, Aldrich). We prepared the counter electrode by applying a 0.7 mM H₂PtCl₆ solution coating onto the FTO substrate. The dye-sensitized TiO₂ electrode films, with an active area of 13–15 mm², were assembled with the counter electrode. The gap distance between the electrodes was fixed at 60 μm using a polymer film spacer (Surlyn, DuPont). The electrolyte solution was then injected into the gap between the two electrodes. The redox couple/electrolyte solution contained 0.05 M LiI (Sigma-Aldrich), 0.03 M I₂ (Yakuri), 0.7 M 1-butyl-3-methylimidazolium iodide (BMII) (Sigma-Aldrich), 0.5 M 4-*tert*-butylpyridine (Aldrich), and 0.1 M guanidine thiocyanate (GSCN) (Wako) dissolved in a solvent mixture of acetonitrile (Aldrich) and valeronitrile (85 : 15 v/v).

Instrumentation and characterization. The surface tension of the PS colloidal solution was measured by the Du Nouy ring method (Sigma 701, Attension). The contact angle was measured using a surface tension analyzer. The surface

morphologies of the meso-IO TiO₂ film were measured by FE-SEM (S-4700, Hitachi). TEM images were obtained using a transmission electron microscope (TEM-3010, JEOL). The amount of dye molecules adsorbed onto each film was measured spectrophotometrically. The N719 dye adsorbed onto the TiO₂ film was detached via immersion in a 0.1 M NaOH solution, and the absorption intensity of the resulting dye solution was measured using a UV-Vis spectrophotometer. The measured intensity was then converted to give a concentration of adsorbed dye molecules. Raman spectra were collected using a Horiba Jobin Yvon LabRAM HR equipped with an air-cooled Ar-ion laser operated at 541 nm. The photocurrent and voltage of the DSCs were measured using a source meter (Keithley Instruments). These measurements were performed under simulated solar illumination produced using a 150 W Xe lamp (Pecell) and AM 1.5G filters. The intensity was calibrated to a power density of 100 mW cm⁻² using a Si reference cell (BS-520, Bunko-Keiki). The electron transit time and recombination lifetime were measured by intensity-modulated photocurrent spectroscopy (IMPS) and intensity-modulated voltage spectroscopy (IMVS), respectively. The measurements were carried out using a frequency response analyzer (XPot, Zahner), which was used to drive a green light-emitting diode (LED) with a wavelength of 520 nm. The LED provided both the DC and AC components of the illumination. The modulation amplitude of the AC component superimposed on the DC component was 10%.

- Gratzel, M. Photoelectrochemical cells. *Nature* **414**, 338–344 (2001).
- Chen, X., Shen, S., Guo, L. & Mao, S. S. Semiconductor-based Photocatalytic Hydrogen Generation. *Chem. Rev.* **110**, 6503–6570 (2010).
- Oregan, B. & Gratzel, M. A low-cost, high-efficiency solar cell based on dye-sensitized colloidal TiO₂ films. *Nature* **353**, 737–740 (1991).
- Nazeeruddin, M. K. *et al.* Conversion of light to electricity by cis-X2bis(2,2'-bipyridyl-4,4'-dicarboxylate)ruthenium(II) charge-transfer sensitizers (X = Cl⁻, Br⁻, I⁻, CN⁻, and SCN⁻) on nanocrystalline titanium dioxide electrodes. *J. Am. Chem. Soc.* **115**, 6382–6390 (1993).
- Hardin, B. E., Snaith, H. J. & McGehee, M. D. The renaissance of dye-sensitized solar cells. *Nature Photon.* **6**, 162–169 (2012).
- Frank, A. J., Kopidakis, N. & van de Lagemaat, J. Electrons in nanostructured TiO₂ solar cells: transport, recombination and photovoltaic properties. *Coord. Chem. Rev.* **248**, 1165–1179 (2004).
- Tetreault, N. & Graetzel, M. Novel nanostructures for next generation dye-sensitized solar cells. *Energ. Environ. Sci.* **5**, 8506–8516 (2012).
- Mor, G. K., Shankar, K., Paulose, M., Varghese, O. K. & Grimes, C. A. Enhanced photocleavage of water using titania nanotube arrays. *Nano Lett.* **5**, 191–195 (2005).
- Law, M., Greene, L. E., Johnson, J. C., Saykally, R. & Yang, P. D. Nanowire dye-sensitized solar cells. *Nature Mater.* **4**, 455–459 (2005).
- Cho, C. Y. & Moon, J. H. Hierarchically Porous TiO₂ Electrodes Fabricated by Dual Templating Methods for Dye-Sensitized Solar Cells. *Adv. Mater.* **23**, 2971–+ (2011).
- Seo, Y. G., Woo, K., Kim, J., Lee, H. & Lee, W. Rapid Fabrication of an Inverse Opal TiO₂ Photoelectrode for DSSC Using a Binary Mixture of TiO₂ Nanoparticles and Polymer Microspheres. *Adv. Funct. Mater.* **21**, 3094–3103 (2011).
- Burke, A. *et al.* The function of a TiO₂ compact layer in dye-sensitized solar cells incorporating “Planar” organic dyes. *Nano Lett.* **8**, 977–981 (2008).
- Guldin, S. *et al.* Dye-Sensitized Solar Cell Based on a Three-Dimensional Photonic Crystal. *Nano Lett.* **10**, 2303–2309 (2010).
- Park, Y., Lee, J. W., Ha, S.-J. & Moon, J. H. 1D nanorod-planted 3D inverse opal structures for use in dye-sensitized solar cells. *Nanoscale* **6**, 3105–3109 (2014).
- Cho, C.-Y., Kim, H.-N. & Moon, J. H. Characterization of charge transport properties of a 3D electrode for dye-sensitized solar cells. *Phys. Chem. Chem. Phys.* **15**, 10835–10840 (2013).
- Melas-Kyriazi, J. *et al.* The Effect of Hole Transport Material Pore Filling on Photovoltaic Performance in Solid-State Dye-Sensitized Solar Cells. *Adv. Energ. Mater.* **1**, 407–414 (2011).
- Snaith, H. J. & Schmidt-Mende, L. Advances in liquid-electrolyte and solid-state dye-sensitized solar cells. *Adv. Mater.* **19**, 3187–3200 (2007).
- Kazim, S., Nazeeruddin, M. K., Graetzel, M. & Ahmad, S. Perovskite as Light Harvester: A Game Changer in Photovoltaics. *Angew. Chem. Int. Ed.* **53**, 2812–2824 (2014).
- Wong, S., Kitaev, V. & Ozin, G. A. Colloidal crystal films: Advances in universality and perfection. *J. Am. Chem. Soc.* **125**, 15589–15598 (2003).
- Kralchevsky, P. A. & Nagayama, K. Capillary interactions between particles bound to interfaces, liquid films and biomembranes. *Adv. Colloid Interf. Sci.* **85**, 145–192 (2000).
- King, J. S., Graugnard, E. & Summers, C. J. TiO₂ inverse opals fabricated using low-temperature atomic layer deposition. *Adv. Mater.* **17**, 1010–+ (2005).
- Schlichthorl, G., Park, N. G. & Frank, A. J. Evaluation of the charge-collection efficiency of dye-sensitized nanocrystalline TiO₂ solar cells. *J. Phys. Chem. B* **103**, 782–791 (1999).
- van de Lagemaat, J. & Frank, A. J. Nonthermalized electron transport in dye-sensitized nanocrystalline TiO₂ films: Transient photocurrent and random-walk modeling studies. *J. Phys. Chem. B* **105**, 11194–11205 (2001).
- Kopidakis, N., Neale, N. R., Zhu, K., van de Lagemaat, J. & Frank, A. J. Spatial location of transport-limiting traps in TiO₂ nanoparticle films in dye-sensitized solar cells. *Appl. Phys. Lett.* **87** (2005).



25. Zhu, K., Kopidakis, N., Neale, N. R., van de Lagemaat, J. & Frank, A. J. Influence of surface area on charge transport and recombination in dye-sensitized TiO₂ solar cells. *J. Phys. Chem. B* **110**, 25174–25180 (2006).
26. Wang, Q. *et al.* Characteristics of high efficiency dye-sensitized solar cells. *J. Phys. Chem. B* **110**, 25210–25221 (2006).
27. Zhu, K., Neale, N. R., Miedaner, A. & Frank, A. J. Enhanced charge-collection efficiencies and light scattering in dye-sensitized solar cells using oriented TiO₂ nanotubes arrays. *Nano Lett.* **7**, 69–74 (2007).
28. Ahmad, S., Guillen, E., Kavan, L., Graetzel, M. & Nazeeruddin, M. K. Metal free sensitizer and catalyst for dye sensitized solar cells. *Energ. Environ. Sci.* **6**, 3439–3466 (2013).

Acknowledgments

This work was supported by grants from the National Research Foundation of Korea (NRF), funded by the Ministry of Science, ICT and Future Planning (2011-0030253). The Korea Basic Science Institute is also acknowledged for the SEM measurements.

Author contributions

J.W.L. designed and conducted overall experiments. J.M.L. and C.Y.C. prepared the organic-dye solar cells. C.H.K. measured the contact angle. J.H.M. supervised the

experiments. J.W.L. and J.H.M. contributed to the interpretation of the data and wrote the article.

Additional information

Supplementary information accompanies this paper at <http://www.nature.com/scientificreports>

Competing financial interests: The authors declare no competing financial interests.

How to cite this article: Lee, J.W., Lee, J., Kim, C., Cho, C.-Y. & Moon, J.H. Facile fabrication of sub-100 nm mesoscale inverse opal films and their application in dye-sensitized solar cell electrodes. *Sci. Rep.* **4**, 6804; DOI:10.1038/srep06804 (2014).



This work is licensed under a Creative Commons Attribution-NonCommercial-NoDerivs 4.0 International License. The images or other third party material in this article are included in the article's Creative Commons license, unless indicated otherwise in the credit line; if the material is not included under the Creative Commons license, users will need to obtain permission from the license holder in order to reproduce the material. To view a copy of this license, visit <http://creativecommons.org/licenses/by-nc-nd/4.0/>